IEEE Access
Multidisciplinary | Rapid Review | Open Access Journal

Received March 3, 2020, accepted March 23, 2020, date of publication March 26, 2020, date of current version April 15, 2020.

Digital Object Identifier 10.1109/ACCESS.2020.2983465

Output Power Stabilization for Wireless Power Transfer System Employing Primary-Side-Only Control

HUANJIE ZHU, BO ZHANG, (Senior Member, IEEE), AND LIHAO WU
School of Electric Power, South China University of Technology, Guangzhou 510641, China

Corresponding author: Bo Zhang (epbzhang@scut.edu.cn)

This work was supported by the Key Program of the National Natural Science Foundation of China under Grant 51437005.

ABSTRACT The output power of a wireless power transfer (WPT) system depends highly on the load and the coupling conditions, which are variable in practical applications generally. In order to attain stable output power with high transfer efficiency under various coupling condition and load, this paper proposes a series-series compensated WPT system based on parity-time (*PT*) symmetry with front-end DC-DC converter and a novel primary-side-only control strategy. The strategy comprises the negative resistance control of *PT*-symmetric circuit, the online load identification approach by *PT*-symmetry, and the power closed-loop control method. The advantages are that the mutual inductance information is not needed, and dual-side wireless communication as well as the secondary-side control circuit is avoided, which compresses the volume of the secondary side, simplifies the control algorithm, and improves the robustness of the system. With the proposed primary-side-only control strategy, the output power is coupling-independent and can automatically stabilize at specified values over reasonable variations both in coupling coefficient and load. The experimental results obtained from a prototype are included. They confirm the proposed control strategy and indicate that system can stably output 200 W and 400 W with the maximum error 4.10% and 3.40% respectively when the coupling coefficient and loads vary, and achieves high overall efficiency at 91.9%.

INDEX TERMS Wireless power transfer (WPT), load identification, coupling-independent, stable output power, high efficiency, parity-time (PT) symmetry.

I. INTRODUCTION

Wireless power transfer (WPT) technology, which allows power transfer from one side to another without any electrical wires, has attracted lots of attention as an alternative technology for domestic and industrial applications in the last two decades due to its critical merit of safety, flexibility and isolation. As a result, the WPT technology has become a research hotspot and has been widely used in many practical areas, ranging from low-power systems such as Internet of Things (IoT), biomedical implantable devices and portable devices charging to medium and high-power systems such as household appliances and charging of electric vehicles(EVs) [1]–[4]. On the other hand, WPT standards, for instance, Qi standard from the Wireless Power Consortium (WPC) and J2954 from the Society of Automotive Engineers (SAE) have been developed to extend the application of the WPT technology further.

The magnetic coupling-based WPT has been one of the most extensively studied methods in WPT technologies. Many pieces of research therein focus on the constant output voltage (CV) and constant output current (CC) charging through complicated control methods or high-order compensations [4], [5] whereas the output power stabilization of the WPT system is also essential in practical applications. Examples of such applications include the WPT systems for constant power charging [6], [7], dynamic charging [8], [9], powering different electrical devices but at a same rated power, and powering constant power load [10], [11]. Besides, the emerging Ki wireless power transfer standard is currently in development for future kitchen applications by WPC [12], enabling the cooking much more precise and responsive. The key is to control the amount of output power for cooking remaining within the limits of the appliance and according to

The associate editor coordinating the review of this manuscript and approving it for publication was Madhav Manjrekar.

the input from users. Therefore, the output power stabilization control is essential in WPT systems. However, for the magnetic coupling-based WPT system, the output power, as well as the transfer efficiency, is sensitive to the variation of the coils' coupling coefficient and the system's load [13], [14]. In practical applications, the coupling coefficient and load are usually uncertain or unfixed. To regulate the output power against the variation of the coupling or load, lots of power control methods have been proposed, which can be classified into primary-side control [1], [15]–[19], secondary-side control [9], [20]–[22] and dual-side control [23]–[25] in general.

A variable capacitance at primary side controlled with a varied duty cycle is proposed to tune frequency for power regulation under a wide variety of load [1]. In Qi standard for commercial product [15], the output power is controlled by altering the frequency of inverter in the range of 110-205 kHz without changing circuit parameters, and a similar method is extended against the variation of distance in [16]. Yet the efficiency decreases with operating frequency deviating from the resonant frequency, and the feedback communication is needed. Therefore, the power-frequency control strategy is developed so as to maintaining high transfer efficiency [17], and a tunable L-type impedance matching network is utilized in [18] to maintain high efficiency under variations both in coil coupling and DC load, but the fluctuation of the output power still occurs when the coupling condition changes. A *PT*-symmetric circuit based on nonlinear gain saturation element is used in primary side to obtain stable efficiency within a specific coupling coefficient range [19], but the load value is fixed and the output power is quite small (19 mW) and efficiency is less than 10%.

As for secondary-side control, authors in [9] proposes an optimal load modulation method by secondary-side boost converter to keep power stable and ensure maximum average transfer efficiency. A buck converter controlled to switch between CCM and DCM is adopted in the secondary side for maximum power transfer tracking [20], but it cannot realize automated regulation when the coupling coefficient varies. Furthermore, the coupling coefficient identification is added to implement automatic control without wireless communication [21], [22], whereas these methods still depend strongly on the information of coupling coefficient and increase the complexity of secondary side. In addition, the overall efficiency is less than 50% when maximum output power achieves.

Dual-side power control strategies via phase-shift control in semi-active rectifier and H-bridge converter are proposed in [23], [24], which dual-side communication is inevitable. To eliminate dual-side wireless communication, authors in [25] adopts front-end load estimation for power tracking control but it is suitable for stationary WPT systems.

Moreover, there are other methods employing multi-coil or multiphase structure for stable output power purpose [26]–[30]. A power control strategy of high-order compensated WPT system with multiphase resonant inverter is put forward in [26], which combines with mutual inductance monitoring, parameter pre-calculation, prediction of several conditions, and the online learning. Authors in [27] propose a parametric optimization method of the coil turns and phase-shifted angles to achieve ZVS for the multiphase resonant inverter, and utilizes cylinder-shaped coils to maintain output power approximately at a constant value. Similar coils are adopted in [28], where the maximum power point is found by parameter identification and the gradient descent method for the stationary and movable cases, respectively. The coordinated control of two source voltages is employed in [29] to deal with the power fluctuation caused by load position variations. In [30], it has been shown that frequency configuration and distribution design of receivers can make the receivers get stable power for WPT systems with single relay and multi-receiver.

Nevertheless, there are several deficiencies in methods mentioned above such as considering only the coupling variation or only the load variation, complicated control algorithm, higher construction cost because of complex system structures, and low reliability due to the wireless communication link. The main objective of this paper is to propose a novel output power control strategy at the primary side for solving the issue of the output power fluctuation caused by the variation both of the coupling coefficient and load in the series-series compensated WPT system. The proposed control strategy is realized by a primary-side controller and an inverter with front-end DC-DC converter, without the need for the information of mutual inductance, wireless communication link, and secondary-side control circuit, thereby compressing the volume of the secondary side, simplifying the control algorithm and improving the robustness of the system. The existing methods in literature fall short in all the above aspects, highlighting the superiority of the proposed control strategy. It involves several elements as follows

1) the negative resistance control for series-series(S-S) compensated WPT system based on parity-time (*PT*) symmetry [31], [32];
2) an online load identification approach employing *PT*-symmetry;
3) the closed-loop control method for the regulation of output power on the basis of the load identification.

The output power of the system using the proposed control strategy is coupling-independent, and can automatically keep stable at desired values under reasonable variation of load.

The rest of this paper consists of four sections. The *PT*-based WPT system and transmission characteristics thereof are analyzed in detail by circuit theory in Section II. In Section III, the system structure is described, and the primary-side-only control strategy is designed. In Section IV, an experimental prototype is fabricated to validate the feasibility of the proposed strategy, and the performance of the designed system is evaluated by associated experimental results. In the last section, the conclusions are drawn from investigation.

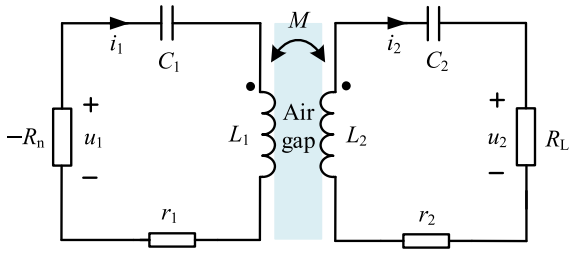

FIGURE 1. Circuit model of series-series compensated WPT system based on *PT*-symmetry.

II. THEORETICAL ANALYSIS OF PT-BASED WPT SYSTEM

A. ANALYSIS VIA CIRCUIT THEORY

The negative resistance plays an essential role in balancing the gain and the loss in the *PT*-symmetry circuit. In contrast to the positive resistance, the negative resistance obeys Ohm's law with a current that flows from low voltage to high voltage, which is the embodiment of time reversal in *PT*-symmetry theory [31]. The circuit model of series-series compensated WPT system based on *PT*-symmetry is shown in Fig. 1, where L_i, C_i, r_i, and i_i (i = 1,2) denote the coil inductance, tuning capacitance, intrinsic loss resistance and current of the primary-side and secondary-side resonators, respectively. M is the mutual inductance between the two coils. The negative resistance $-R_n$ is the only gain element in the system that provides power to the primary LC loop. Through the magnetic coupling between the primary-side coil and secondary-side coil, the power transfers to the secondary-side loss elements, i.e. r_2 and load R_L. The reference positive direction of i_1 and i_2 are shown by the arrows in Fig. 1. The AC voltage u_1 of negative resistance is in phase with i_1, and u_2 is the output voltage, i.e. the voltage of AC load R_L.

The *PT*-based WPT system has been analyzed via coupled-mode theory in our previous work [33]. In this paper, the circuit theory and fundamental harmonic analysis (FHA) are applied to model the *PT*-based WPT system to acquire the electrical expression of steady transmission characteristics. Considering the fundamental harmonic of voltage and current, u_1, u_2, i_1, and i_2 can be easily expressed in terms of phasors $\dot{U}_1$, $\dot{U}_2$, $\dot{I}_1$ and $\dot{I}_2$, respectively. For the circuit model in Fig. 1, according to Kirchhoff's voltage law, the voltage equations of the primary-side and secondary-side circuits can be derived as

$$\begin{cases} (-R_n + r_1)\,\dot{I}_1 + \left(j\omega L_1 - j\dfrac{1}{\omega C_1}\right)\dot{I}_1 - j\omega M\dot{I}_2 = 0 \\ -j\omega M\dot{I}_1 + (R_L + r_2)\,\dot{I}_2 + \left(j\omega L_2 - j\dfrac{1}{\omega C_2}\right)\dot{I}_2 = 0, \end{cases} \tag{1}$$

where j is the imaginary unit, and ω is the operating angular frequency of the system. k denotes the coupling coefficient and $k = M/\sqrt{L_1L_2}$. Then we rewrite (1) into matrix form as

$$\begin{pmatrix} \dfrac{1}{\omega L_1C_1} - \omega + j\dfrac{-R_n + r_1}{L_1} & \omega k\sqrt{\dfrac{L_2}{L_1}} \\ \omega k\sqrt{\dfrac{L_1}{L_2}} & \dfrac{1}{\omega L_2C_2} - \omega + j\dfrac{R_L + r_2}{L_2} \end{pmatrix} \begin{pmatrix} \dot{I}_1 \\ \dot{I}_2 \end{pmatrix} = 0. \tag{2}$$

Let the natural angular frequency of the primary-side and secondary-side circuits be $\omega_1 = \omega_2 = \omega_0$, i.e. $\omega_0 = 1/\sqrt{L_1C_1} = 1/\sqrt{L_2C_2}$, which is one of the *PT*-symmetric conditions. Therefore, (2) can be furthered derived as

$$\begin{pmatrix} \dfrac{\omega_0}{\omega} - \dfrac{\omega}{\omega_0} + j\dfrac{-R_n + r_1}{\omega_0 L_1} & \dfrac{\omega}{\omega_0}k\sqrt{\dfrac{L_2}{L_1}} \\ \dfrac{\omega}{\omega_0}k\sqrt{\dfrac{L_1}{L_2}} & \dfrac{\omega_0}{\omega} - \dfrac{\omega}{\omega_0} + j\dfrac{R_L + r_2}{\omega_0 L_2} \end{pmatrix} \begin{pmatrix} \dot{I}_1 \\ \dot{I}_2 \end{pmatrix} = 0, \tag{3}$$

which has nontrivial solutions only if the coefficient matrix has a zero determinant

$$\left(\frac{\omega_0}{\omega} - \frac{\omega}{\omega_0} + j\frac{-R_n + r_1}{\omega_0 L_1}\right)\left(\frac{\omega_0}{\omega} - \frac{\omega}{\omega_0} + j\frac{R_L + r_2}{\omega_0 L_2}\right) - \left(\frac{\omega k}{\omega_0}\right)^2 = 0. \tag{4}$$

The real and imaginary part of (4) can be separated respectively as

$$\left(\frac{\omega_0}{\omega} - \frac{\omega}{\omega_0}\right)^2 - \left(\frac{\omega k}{\omega_0}\right)^2 - \frac{(-R_n + r_1)(R_L + r_2)}{\omega_0^2 L_1 L_2} = 0\,, \tag{5}$$

$$\left(\frac{\omega_0}{\omega} - \frac{\omega}{\omega_0}\right)\left(\frac{-R_n + r_1}{\omega_0 L_1} + \frac{R_L + r_2}{\omega_0 L_2}\right) = 0. \tag{6}$$

From (5) and (6), two cases are discussed as follows.

1) $\omega \neq \omega_0$

When $\omega \neq \omega_0$, the R_n will automatically meet

$$\frac{-R_n + r_1}{L_1} + \frac{R_L + r_2}{L_2} = 0\,, \tag{7}$$

and ω satisfies

$$\omega = \omega_\pm = \omega_0\sqrt{\frac{A \pm \sqrt{A^2 + 4\left(k^2 - 1\right)}}{2\left(1 - k^2\right)}}\,, \tag{8}$$

in which

$$A = 2 - \left(\frac{R_L + r_2}{\omega_0 L_2}\right)^2.$$

So as to obtain the solution of (3) with a real ω while allowing R_L or k to vary, the system ought to satisfy following conditions

$$\begin{cases} A^2 + 4\left(k^2 - 1\right) \geq 0 \\ A \pm \sqrt{A^2 + 4\left(k^2 - 1\right)} \geq 0 \end{cases}, \tag{9}$$

where $0 \leq k \leq 1$. Thus, the condition can be derived as

$$R_L \leq R_C = \omega_0 L_2\sqrt{2\left(1 - \sqrt{1 - k^2}\right)} - r_2\,, \tag{10}$$

where R_C is the critical load resistance. In this condition, the system is *PT*-symmetric.

2) $\omega = \omega_0$

When $\omega = \omega_0$, from (5) and (6) the R_n can be derived as

$$-R_n = -\frac{L_1 L_2 \omega_0^2 k^2}{(R_L + r_2)} - r_1 \,. \tag{11}$$

In this case, the *PT*-symmetry of the system is broken.

From(10), it can be observed that the load can be divided into two parts: $R_L \le R_C$ and $R_L > R_C$. From the viewpoint of physical meaning, the two parts correspond to the exact *PT*-symmetric region and the broken *PT*-symmetric region, respectively [19], [32]. We note that $\omega = \omega_0$ is also a solution of (3), but it is unstable in the exact *PT*-symmetric region [19]. Therefore, the operating frequency f of the system can be derived as

$$f = \begin{cases} f_0 \sqrt{\dfrac{B \pm \sqrt{B^2 + 4\left(k^2 - 1\right)}}{2\left(1 - k^2\right)}} & (R_L \le R_C) \\ f_0 & (R_L > R_C) \end{cases}, \tag{12}$$

where the frequency $f_0 = \omega_0 / 2\pi$, and

$$B = 2 - \left(\frac{R_L + r_2}{2\pi f_0 L_2}\right)^2 \,.$$

As can be seen from (12), in the exact *PT*-symmetric region, a bifurcation of the system's operating frequency occurs and two frequency branches exist, i.e., the high-frequency branch and the low-frequency branch, respectively. In the broken *PT*-symmetric region, the operating frequency of the system is the natural frequency f_0.

B. TRANSMISSION CHARACTERISTICS

The transmission characteristics of *PT*-based WPT system, such as the current ratio of the primary side and secondary side, transfer efficiency η, and power P_L delivered to the load can be derived from the above analysis.

Substituting (5) and (7) into (3) in the exact *PT*-symmetric region yields the current ratio as

$$\frac{I_1}{I_2} = \sqrt{\frac{L_2}{L_1}} \,, \tag{13}$$

where I_1 and I_2 are the root-mean-square (RMS) value of fundamental components of i_1 and i_2, respectively. Meanwhile, the ratio of phasor $\dot{I}_1$ and $\dot{I}_2$ is deduced as

$$\frac{\dot{I}_1}{\dot{I}_2} = \sqrt{\frac{L_2}{L_1}} \left(\frac{1 - f_0^2/f^2}{k} - j\frac{R_L + r_2}{2\pi f L_2 k}\right) \,. \tag{14}$$

Thus, the phase difference between i_1 and i_2 is derived as

$$\varphi_1 - \varphi_2 = \begin{cases} \arctan \dfrac{f\,(R_L + r_2)}{2\pi\left(f_0^2 - f^2\right) L_2} & f > f_0 \\ -\pi + \arctan \dfrac{f\,(R_L + r_2)}{2\pi\left(f_0^2 - f^2\right) L_2} & f < f_0 \end{cases}, \tag{15}$$

where the φ_1 and φ_2 are the phase angles of $\dot{I}_1$ and $\dot{I}_2$, respectively. The phase difference is related to the load and operating frequency.

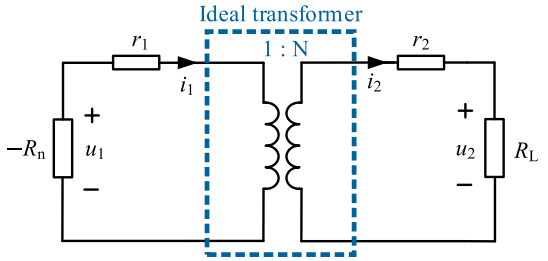

FIGURE 2. Equivalent circuit of the exact *PT*-symmetric region (the phase relation of i_1 and i_2 is neglected).

As for the broken *PT*-symmetric region, $f = f_0$ and (11) are substituted into equation (3) to obtain the current ratio as

$$\frac{I_1}{I_2} = \frac{R_L + r_2}{2\pi f_0 k \sqrt{L_1 L_2}} \,, \tag{16}$$

and the phase difference $\varphi_1 - \varphi_2 = t\pi/2$. In general, the transfer efficiency of the series-series compensated WPT system is expressed as [34]

$$\eta = \frac{I_2^2 R_L}{I_1^2 r_1 + I_2^2 R_L + I_2^2 r_2} \,. \tag{17}$$

The expression of η in the exact *PT*-symmetric region and the broken *PT*-symmetric region can be obtained for the *PT*-based WPT system by substituting (13) and (16) into (17), respectively

$$\eta = \begin{cases} \dfrac{R_L}{\dfrac{L_2}{L_1} r_1 + r_2 + R_L} & (R_L \le R_C) \\ \dfrac{4\pi^2 R_L f_0^2 k^2 L_1 L_2}{r_1 (R_L + r_2)^2 + (r_2 + R_L)\, 4\pi^2 f_0^2 k^2 L_1 L_2} & (R_L > R_C). \end{cases} \tag{18}$$

The negative resistance $-R_n$ satisfies

$$I_1 R_n = U_1 \,, \tag{19}$$

where the U_1 is the RMS value of fundamental components u_{1_FHA} of u_1. The output power P_L can be generally given by

$$P_L = I_2^2 R_L \,. \tag{20}$$

Furthermore, the output power P_L of the *PT*-based WPT system in the exact *PT*-symmetric region can be deduced by substituting (7) and (13) into (19) and (20):

$$P_L = \frac{R_L U_1^2}{\frac{L_1}{L_2}(R_L + r_2)^2 + 2 r_1 (R_L + r_2) + \frac{L_2}{L_1} r_1^2}, (R_L \le R_C). \tag{21}$$

The output power P_L of the *PT*-based WPT system in the broken *PT*-symmetric region can be derived by substituting (11) and (16) into (19) and (20):

$$P_L = \frac{4\pi^2 f_0^2 k^2 L_1 L_2 R_L U_1^2}{\left[4\pi^2 f_0^2 k^2 L_1 L_2 + r_1 (R_L + r_2)\right]^2} \quad (R_L > R_C). \tag{22}$$

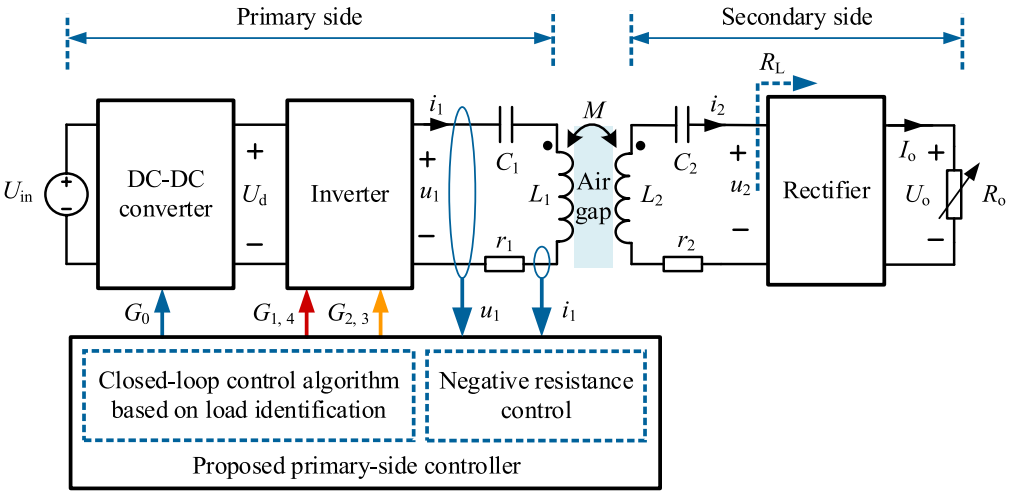

FIGURE 3. System structure of the proposed WPT system.

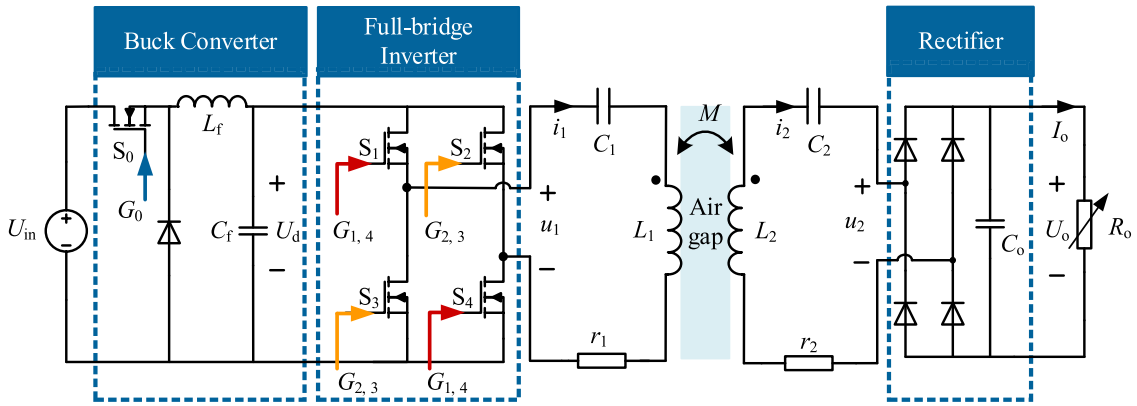

FIGURE 4. Main circuit of the proposed WPT system.

From (13), (18), and (21), the equivalent circuit of the exact *PT*-symmetric region is obtained when the phase relation of $\dot{I}_1$ and $\dot{I}_2$ is neglected. As shown in Fig. 2, the equivalent circuit of the exact *PT*-symmetric region comprises an ideal transformer that ratio is 1:N, where $\mathrm{N} = \sqrt{L_2}/L_1$. It can be seen that the current ratio, the output power P_L and the transfer efficiency η are independent on the coupling coefficient k in the exact *PT*-symmetric region, which is superior compared with transfer characteristics of magnetic resonant WPT system.

III. PROPOSED SYSTEM STRUCTURE AND PRIMARY-SIDE-ONLY CONTROL STRATEGY

In this section, the proposed system structure and its analysis are presented. Then, based on the circuit analysis of the system, the output power stabilization control strategy for the primary-side controller is designed.

A. SYSTEM STRUCTURE AND SECONDARY-SIDE RECTIFIER MODEL

The WPT system consists of two insulated parts named as primary side and secondary side. When the load resistance is relatively small, rather than the kilo-ohm level, the series-series topology is more appropriate to output more power, so that both primary side and secondary side are series-series compensation in this system. The proposed system structure is shown in Fig. 3, while the detailed circuit is depicted in Fig. 4.

The front-end DC-DC converter, which could be a buck, boost or buck-boost converter, is utilized to regulate the input voltage U_d of the inverter at the primary side for output power stabilization control. The buck converter is employed in this paper, and U_d is given by

$$U_\mathrm{d} = DU_\mathrm{in}\ , \tag{23}$$

where U_in is the voltage of the DC power source, and D is the duty cycle.

The full-bridge inverter, which is a voltage-source-type inverter (VSI) and widely used in WPT systems due to their high voltage utilization and simplicity, is adopted to realize the ac negative resistance in this paper. Then, the output power stabilization control based on primary-side information is realized only by the proposed primary-side controller, which consists of the negative resistance control, load identification and output power closed-loop control. As can be

seen from Fig. 3, the system does not have dual-side wireless communication and secondary-side control circuits, which compresses the volume of the secondary side.

On the secondary side, through the full-bridge rectifier with capacitive output filter, the obtained AC voltage u_2 is converted to DC voltage U_o for household applications, battery charging and other power converters *et al*. The purpose of this paper is to propose and verify a WPT system and its output power stabilization control strategy so that the DC resistance is used as the load in analysis. As shown in Fig. 4, the secondary-side rectifier connects with the output filter C_o. The input voltage u_2 and the current i_2 of the rectifier are square and sine wave, respectively. In practice, only the fundamental harmonic of voltage and current is considered for simplicity during the analysis of the WPT system. Thus, the output DC current I_o is expressed as

$$I_o = \frac{1}{\pi}\int_0^{\pi} \sqrt{2} I_2 \sin(\omega t)\, d(\omega t) = \frac{2\sqrt{2}}{\pi} I_2 , \qquad (24)$$

where I_2 is the RMS value of fundamental harmonic of secondary-side current i_2. The load resistance in the WPT system may change with the operating condition of the practical application generally. Assuming that the rectifier power losses are ignored in the following derivation, the energy conservation equation is given by

$$I_o^2 R_o = I_2^2 R_L , \qquad (25)$$

where R_o is the equivalent DC load resistance and R_L is the equivalent input resistance seen into the full-bridge rectifier with output filter C_o. From (24) and (25), R_L and I_2 are deduced as follows, respectively:

$$R_L = \frac{8}{\pi^2} R_o , \qquad (26)$$

$$I_2 = \frac{\pi}{2\sqrt{2}} I_o . \qquad (27)$$

B. NEGATIVE RESISTANCE CONTROL

According to the property of negative resistance, it is feasible to control the output voltage u_1 in phase with the output current i_1 of the VSI by using the current i_1 in the primary-side resonant tank as a feedback signal merely. Therefore, this self-oscillating controlled VSI can be equivalent to a negative resistance, and the control circuit thereof is depicted in Fig. 5.

The primary-side current i_1, i.e., the output current of the VSI, is captured via current sense transformer and converted into the voltage signal. Then the voltage signal is amplified by the differential amplifier and send to zero-crossing comparator via a time-leading compensator to detect the zero-crossing points of i_1. Finally, the output signal of the comparator is sent to dead time generation circuit to generate pulse width modulation (PWM) signals, i.e., $PWM_{G1,4}$ and $PWM_{G2,3}$, which drive the corresponding switch S_1-S_4 of the full-bridge inverter in Fig. 4, to make u_1 keep in phase with i_1. The time-leading compensator after the amplifier is used for compensating the time delay of the current sense transformer, zero-crossing comparator, dead time circuit and drivers,

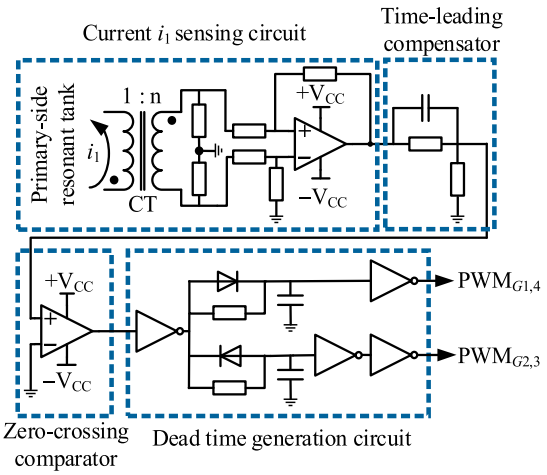

FIGURE 5. Self-oscillating control circuit diagram of the full-bridge inverter for negative resistance.

to ensure that u_1 is in phase with i_1. By this self-regulated control circuit, the system can self-track the operating frequency in (12) constantly to ensure working in the *PT*-symmetry region, without the need for active tuning using the information of coupling coefficient k and load resistance.

The output waveforms and PWM signals of the full-bridge inverter by the negative resistance control are shown in Fig.6. The duty width of the PWM signals for switch S_1-S_4 are 50% without considering the dead time. The output current i_1 of the VSI is almost sinusoidal wave due to the high intrinsic quality factor (Q) of the primary-side resonant tank, while the output voltage u_1 is a square wave. Through the control circuit, both u_1 and its fundamental harmonic u_{1_FHA} are in phase with the output current i_1, which is consistent with the property of negative resistance. Based on FHA, the RMS value U_1 of u_{1_FHA} is given by

$$U_1 = \frac{2\sqrt{2}}{\pi} U_d . \qquad (28)$$

It can be seen that the voltage of the negative resistance can be regulated easily by adjusting the output voltage of the front-end buck converter.

C. ONLINE LOAD IDENTIFICATION APPROACH

In practical applications, the equivalent resistive load R_o that calculated by U_o/I_o may be uncertain or variable. In order to control the output power only by the primary-side controller, it is necessary to identify the load R_o indirectly in real time.

The property of *PT*-symmetric circuit indicates that R_o has a relationship with the negative resistance $-R_n$, so it is possible to estimate R_o employing primary-side information. Therefore, a novel online load identification approach by *PT*-symmetry is proposed.

From (7), the R_L is derived as

$$R_L = \frac{L_2}{L_1}(R_n - r_1) - r_2 . \qquad (29)$$

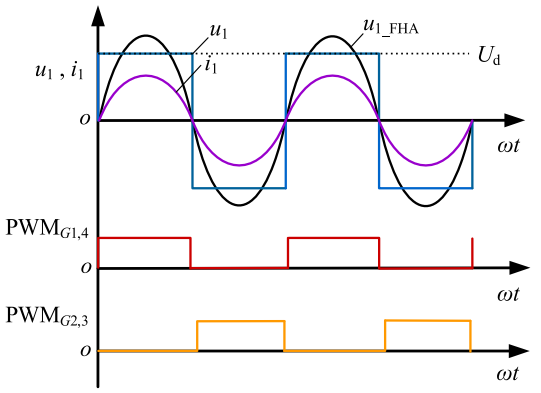

FIGURE 6. PWM signals and output waveforms of the full-bridge inverter.

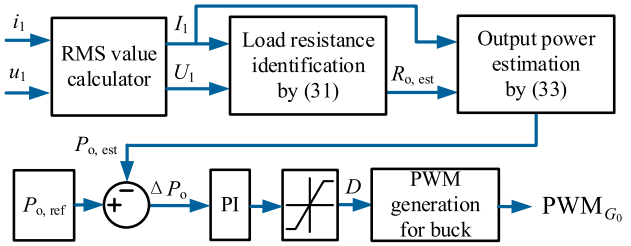

FIGURE 7. Control block diagram of the proposed closed-loop control method.

Then, the load R_o can be deduced by substituting (26) into (29):

$$R_o = \frac{\pi^2}{8}\left[\frac{L_2}{L_1}(R_n - r_1) - r_2\right]. \tag{30}$$

Obviously, combining (19) and (30), the estimated value $R_{o,\,est}$ of the load R_o is calculated by

$$R_{o,\,est} = \frac{\pi^2}{8}\left[\frac{L_2}{L_1}\left(\frac{U_1}{I_1} - r_1\right) - r_2\right]. \tag{31}$$

Once the system is fabricated, the circuit parameters, i.e. the values of L_i and r_i ($i = 1,2$) are acquired by the previous measurement and assumed to be constant approximately. Therefore, through acquiring and calculating the RMS values of U_1 and I_1 in real time without the need for complicated measuring of the phase or active power [5], [25], the estimated value $R_{o,\,est}$ can be quickly obtained according to (31) in the exact *PT*-symmetric region, which is easy to implement in the digital processor.

D. OUTPUT POWER CLOSED-LOOP CONTROL METHOD

As transmission characteristics shown in Section II-B, the output power is coupling-independent and only related to the voltage U_1 and the load R_L in the exact *PT*-symmetric region.

With (21), (23) and (28), the output power P_L is deduced as

$$P_L = \frac{\frac{8}{\pi^2}U_{in}^2 D^2 R_L}{\frac{L_1}{L_2}(R_L + r_2)^2 + 2r_1(R_L + r_2) + \frac{L_2}{L_1}r_1^2}. \tag{32}$$

It indicates that the voltage of negative resistance can be adjusted according to the load resistance identification results, and the desired output power P_L is achieved consequently, while the information of the coupling coefficient is not required. Therefore, the closed-loop control of the output voltage of the front-end DC-DC converter is essential to achieve the accurate and robust output power control when the load varies. Assuming that the rectifier power losses are ignored, the output power $P_o = I_o U_o = P_L$. Since there is no wireless communication desired in the system, the output power P_o should be estimated based on the load identification in Section III-C. From(13), (20), and(26), the estimated value $P_{o,\,est}$ of output power is calculated by

$$P_{o,\,est} = \frac{8L_1}{\pi^2 L_2} I_1^2 R_{o,\,est}. \tag{33}$$

Finally, a closed-loop PI control method is proposed for output power regulation in the exact *PT*-symmetric region. As described in Fig. 7, the closed-loop control block diagram consists of the online load identification, the output power estimation, and the PWM signal generation of PI-controlled buck converter. While the load varies, through acquiring the output current i_1 and the output voltage u_1 in real time and calculating RMS value of fundamental harmonic respectively, the DC load resistance and the output power can be estimated using (31) and (33). The estimated values P_o, est is compared with a preset reference $P_{o,\,ref}$, which represents the desired output power P_o. The error $\Delta P_o = P_{o,\,ref} - P_o$, est is fed into the PI controller that generates the duty cycle D, and the switch driver generates the PWM signal that drives the buck converter. Eventually, the voltage U_1 of negative resistance is regulated to maintain constant P_o. Obviously, the proposed control method in the exact *PT*-symmetric region is coupling-independent, which simplifies the control algorithm and improves the robustness of the system.

With the proposed output power stabilization control strategy, the normalized output power and corresponding transfer efficiency as the function of coupling coefficient k and load resistance R_o are theoretically calculated and plotted in Fig. 8. The circuit parameters are listed in Table 1. The critical line in Fig. 8(a) is the boundary of the exact *PT*-symmetric region constrained by (10). The simulation results indicate that the output power can stabilize at specified levels against variations both of the load and coupling coefficient via the proposed control strategy, meanwhile, the transfer efficiency is also coupling-independent in the exact *PT*-symmetric region and the greater the DC load R_o, the higher the transfer efficiency, which is show shown in Fig. 8(b). Moreover, by substituting (31) into (33) and simplifying, it can be seen that the output power estimation is still correct in broken PT-symmetric region if the loss resistance r_2 can be neglected, thus the output power control strategy will still be feasible in broken *PT*-symmetric region.

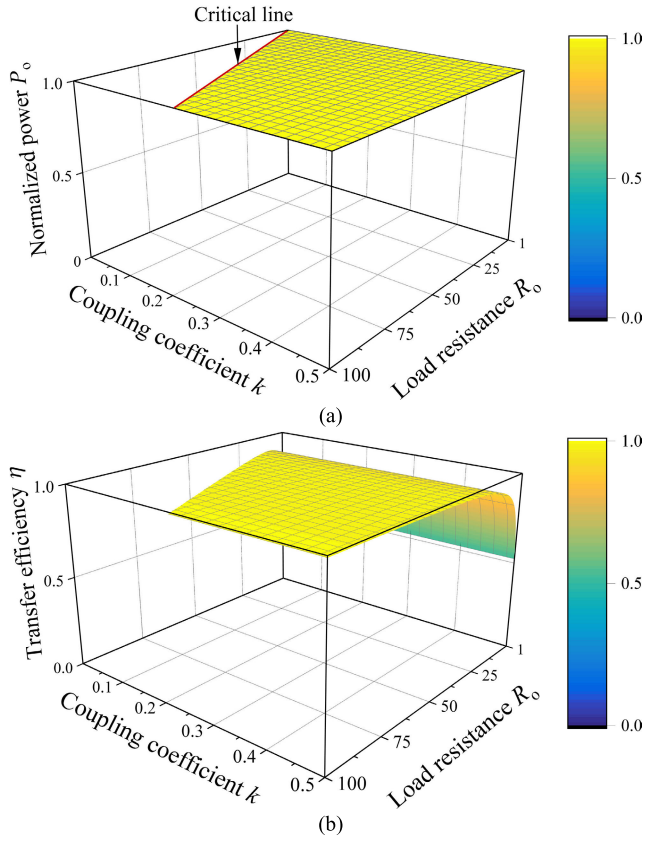

FIGURE 8. Output results of numerical simulation under various condition by the proposed output power stabilization control strategy: (a) normalized output power; (b) transfer efficiency.

TABLE 1. Parameters of the experimental prototype.

Symbol	Note	Values
L_1	Inductance in primary-side resonator	192.83 μH
L_2	Inductance in secondary-side resonator	193.20 μH
C_1	Series capacitance in primary-side resonator	1.519 nF
C_2	Series capacitance in secondary-side resonator	1.518 nF
r_1	AC loss resistance in primary-side resonator	0.361 Ω
r_2	AC loss resistance in secondary-side resonator	0.366 Ω
f_{10}	Resonant frequency of primary-side resonator	294 kHz
f_{20}	Resonant frequency of secondary-side resonator	294 kHz
U_{in}	DC input voltage of system	180 V
L_f	Inductance of front-end buck converter	1.8 mH
U_f	Forward voltage of rectifier diode	0.86 V at 20 A
C_o	Output filter capacitance of rectifier	220 μF/250 V

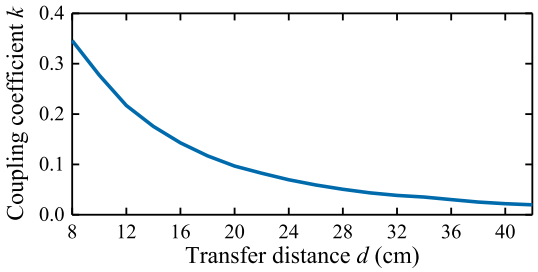

FIGURE 9. Measured coupling coefficient with respect to the transfer distance between the two coaxially-aligned coils.

IV. EXPERIMENTAL VALIDATION

On the basis of the above-mentioned analysis, the experimental prototype has been designed and fabricated in this section to evaluate the performance of the WPT system with the proposed primary-side-only control strategy.

A. EXPERIMENTAL SETUP

For the coreless coils of resonators, the helix shape coil made by Litz wire (ϕ 0.05 mm × 1000 strands, outer ϕ 2.3 mm) is chosen considering the skin effect at several hundred kilohertz. The diameter of each coil is 30 cm and the axial width is about 6 cm with single layer 20-turn (axial arrangement) structure. For the series capacitors of resonators, the high voltage doorknob ceramic capacitors are chosen for their low losses and high current-bearing capability at high frequency. The circuit parameters of resonators measured by a precise impedance analyzer (Wayne Kerr 6500B) are listed in Table 1. The frequency sweeping measurement results indicate that the loss resistances of resonators vary little within 250-350 kHz, so they are considered constant in the analysis, which are equal to the values shown in Table 1. When the distance between the two coils changes, the variation of the coupling coefficient is measured and shown in Fig. 9.

Fig. 10 shows the experimental prototype. Starting from the DC voltage source, the power flows through the front-end buck converter (MOSFET: Infineon IRFP4227PBF, and Schottky diode: ON MBR40250TG), the full-bridge inverter (MOSFETs: Infineon BSC350N20), a pair of magnetically coupled resonators, the rectifier (Schottky diodes: ON MBR40250) and capacitive filter (film capacitor). Finally, it is provided to load resistors (Chroma DC electronic load). In the primary-side controller, the output current of the VSI is converted into the voltage signal by a current sense transformer CU8965, and then the voltage signal passes through the control signal generation circuit consisting of the high-speed operational amplifier LM6172, the zero-crossing comparator TL3016 and the dead time generation circuit containing a quad-2 input NAND gate (Fairchild 74VHC00MTCX). PWM signals drive the switch S_0-S_4 via isolated gate drivers (Silabs Si8271). A floating-point digital-signal processor TMS320F28377d is employed to sample the RMS value via an RMS calculator AD637 and carry out the output power closed-loop control.

Note that the electronic components can be selected by actual demands such as cost, control speed and power capacity in different practical applications. Moreover, the minimum coupling coefficient k of the system can be preset according to the range of the practical load by (10).

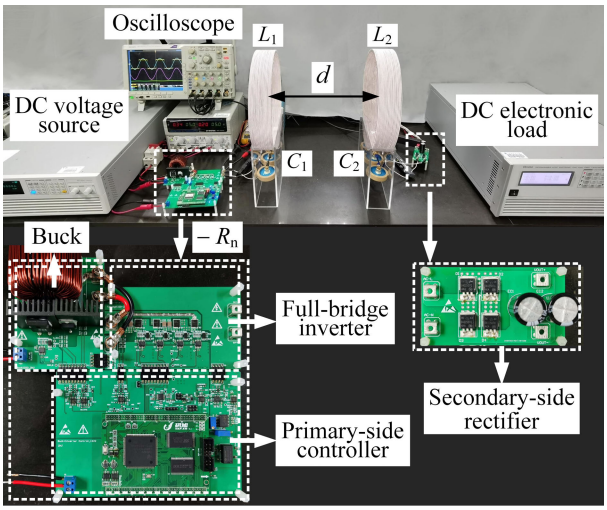

FIGURE 10. Photo of the designed experimental prototype.

Actually, many other WPT systems have to work in preset range as well [5], [18]–[30]. The coreless coil in this paper has not been optimally designed because the experimental setup mainly focuses on providing proof of propose strategy rather than an actual product. System performance can be further improved by optimizing coil design or using ferrite cores.

B. EXPERIMENTAL RESULTS OF PROPOSED SYSTEM AND CONTROL STRATEGY

First, the prototype is tested in different coupling conditions to validate the transmission characteristics analyzed in Section II. The reference output power $P_{\mathrm{o,ref}}$ =400 W, and the DC electronic load is set to 15 Ω, i.e., R_{o} = 15 Ω. Under this condition, the critical coefficient k = 0.036. Experimental and calculated results are shown in Fig. 11. The actual output power P_{o} is read from the DC electronic load directly, and the transfer efficiency is defined by (17). As can be seen from Fig. 11(a), the output power nearly stabilizes at the reference level with the power error Δ_P ($\Delta_P = \left|P_{\mathrm{o}} - P_{\mathrm{o,ref}}\right| / P_{\mathrm{o,ref}}$) less than 2.85% over the coupling coefficient ranging from 0.35 to 0.036. The experimental results in Fig. 11(b) indicate that the transfer efficiency (around 95%), as well as the current ratio, remains almost constant within a range of 34 cm (k = 0.036−0.35). The operating frequency f and the phase difference $\varphi_1 - \varphi_2$ of currents measured by the oscilloscope are displayed in Fig. 11(c), which show that the experimental prototype operates at the low-frequency branch, and $\varphi_1 - \varphi_2$ gradually increases and approaches $t\pi/22$ as d increases. The experimental results coincide with calculated values in the exact *PT*-symmetric region.

To validate the output power stabilization control strategy, the system controlled by the primary-side controller is tested under different load and coupling coefficient with reference output power $P_{\mathrm{o,ref}}$ = 200 W and 400 W, respectively. Transfer distance d = 15 cm and 20 cm correspond coupling coefficient k = 0.15 and 0.096, respectively.

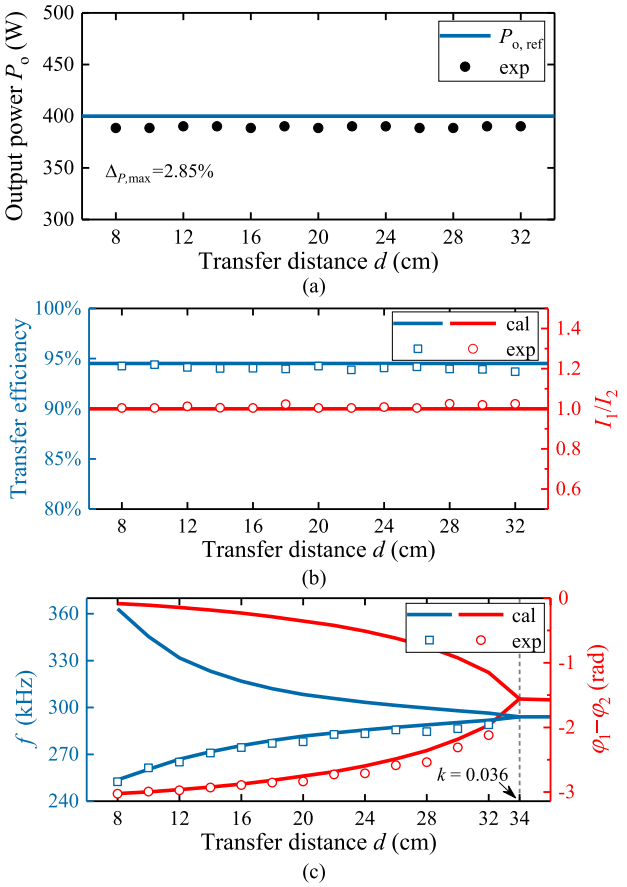

FIGURE 11. Experimental results of $P_{\mathrm{o,ref}}$ = 400 W and R_{o} = 15Ω under different transfer distance *d*: (a) output power; (b) transfer efficiency and current ratio; (c) operating frequency and phase differences of i_1, i_2.

TABLE 2. Experimental results of online load identification.

R_{o} (Ω)	d = 15 cm (k = 0.15)		d = 20 cm (k = 0.096)	
	$R_{\mathrm{o,est}}$ (Ω)	Δ_R	$R_{\mathrm{o,est}}$ (Ω)	Δ_R
10	10.43	4.25%	10.40	4.01%
15	15.61	4.03%	15.52	3.45%
20	20.55	2.73%	20.51	2.55%
25	26.07	4.26%	25.79	3.14%
30	31.00	3.33%	30.85	2.85%
35	36.22	3.47%	36.10	3.14%
40	40.95	2.37%	41.00	2.50%

Through acquiring and calculating the RMS value U_1 and I_1, the load R_{o} can be easily estimated by the proposed online load identification approach. Table 2 shows experimental results of $R_{\mathrm{o,est}}$ and the corresponding error Δ_R ($\Delta_R = \left|R_{\mathrm{o,est}} - R_{\mathrm{o}}\right| / R_{\mathrm{o}}$) when $P_{\mathrm{o,ref}}$ = 200 W. The error Δ_R is less than 4.3% under k = 0.15 and 0.096, which decreases with the increase of R_{o}. The average value of $R_{\mathrm{o,est}}$ can be used to reduce the errors.

Experimental results and waveforms of $P_{\mathrm{o,ref}}$ = 200 W are shown in Fig. 12 and Fig. 13, respectively. It indicates that the output power P_{o} can be stable at the desired value against various loads under k = 0.15 or k = 0.096. The maximum error Δ_P is 4.10% corresponding to output power 191.8 W

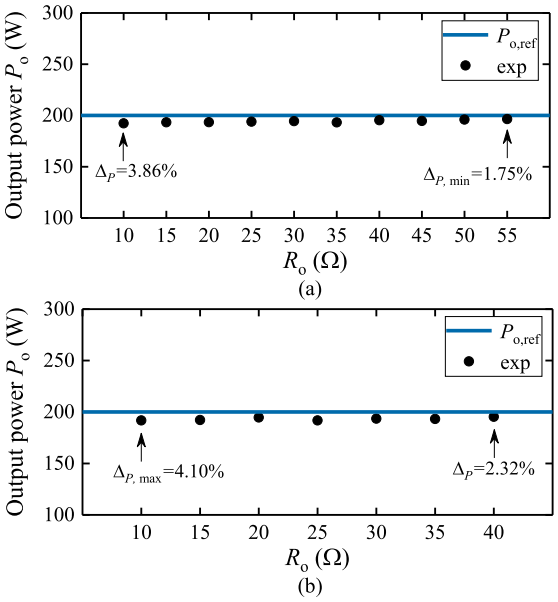

FIGURE 12. Experimental results of output power and errors when $P_{o,ref}$ = 200 W under different load R_o: (a) d = 15 cm; (b) d = 20 cm.

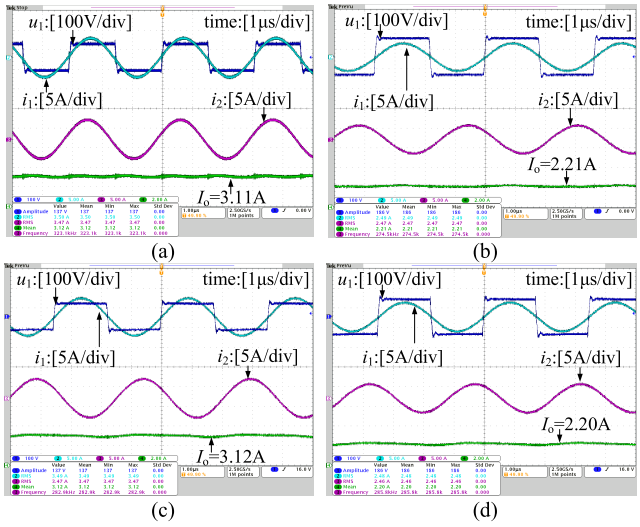

FIGURE 13. Experimental waveforms when $P_{o,ref}$ = 200 W under different conditions: (a) R_o = 20Ω, d = 15 cm; (b) R_o = 40Ω, d = 15 cm; (c) R_o = 20Ω, d = 20 cm; (d) R_o = 40Ω, d = 20 cm.

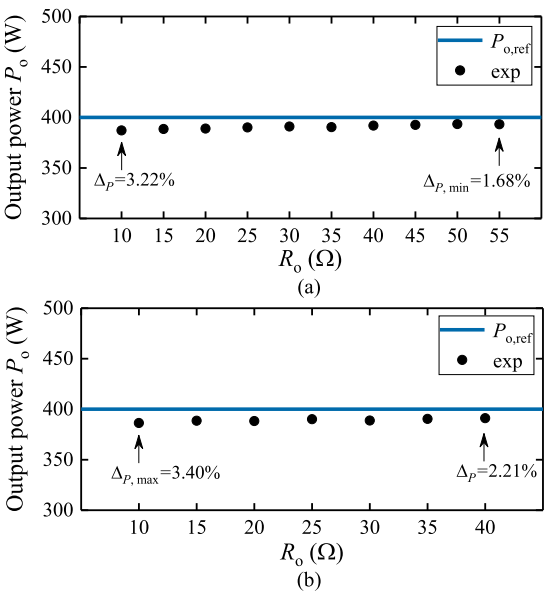

FIGURE 14. Experimental results of output power and errors when $P_{o,ref}$ = 400 W under different load R_o: (a) d = 15 cm; (b) d = 20 cm.

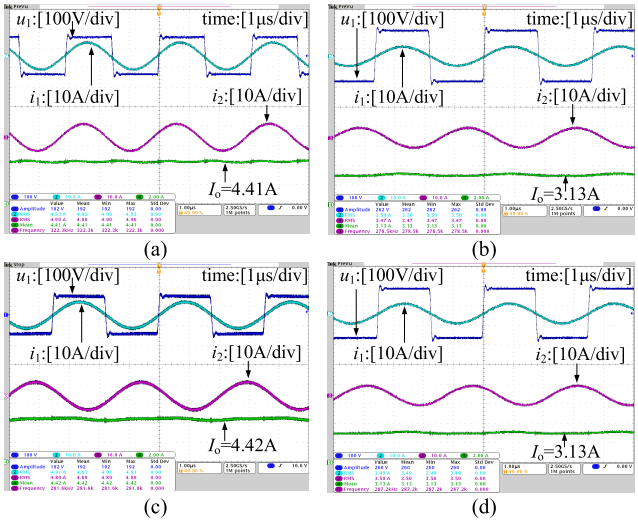

FIGURE 15. Experimental waveforms when $P_{o,ref}$ = 400 W under different conditions: (a) R_o = 20Ω, d = 15 cm; (b) R_o = 40Ω, d = 15 cm; (c) R_o = 20Ω, d = 20 cm; (d) R_o = 40Ω, d = 20 cm.

at R_o = 10Ω, while the minimum error Δ_P is 1.75% corresponding to output power 196.5 W at R_o = 55Ω. Similarly, the output power can also be controlled at $P_{o,ref}$ = 400 W under different loads and coupling coefficients, experimental results and waveforms of which are shown in Fig. 14 and Fig.15. Experimental results show that the maximum error Δ_P is 3.40% corresponding to output power 386.4 W at R_o = 10Ω, while the minimum error Δ_P is 1.68% corresponding to output power 393.3 W at R_o = 55Ω.

As can be seen from the experimental waveforms, the working frequency self-regulates at different operating points by the negative resistance control, but there are minor phase differences between the current i_1 and voltage u_1 at certain operating points, which are caused by the variation of leading time of the compensator at the different operating frequency. The VSI can be regarded approximately as a negative resistance since the errors are quite small and experimental results nearly correspond to the theory. The digital control will be explored further in our future work to help controlling the system to work at low frequency branches. The voltage u_1 will automatically change to sustain stable output power at each operating point without using the information of coupling coefficient k. The output power error Δ_P tends to decrease as the load resistance R_o increases. The experimental results indicate that output power is stable when the loads and coupling coefficients vary, which validates the correctness of proposed output power stabilization control strategy.

TABLE 3. Reported WPT prototypes with output power stabilization control methods.

Reference	Coupler	Range of coupling coefficient k	Resonant frequency (kHz)	Overall efficiency	Power (W)	Operating condition	Manner	Information of mutual inductance
[18]	Double coils (S-S) Without ferrite	0.1–0.4	6780	80%	9	Preset points	Primary-side control	Need
[20]	Double coils (S-S) With ferrite	0.3–0.4	40	44%	80	Variable	Secondary-side control	Need
[26]	Double coils (LCL-S) Without ferrite	– –	85	87.4%	60	Fixed load	Primary-side control	Need
[29]	Three coils (S-S-S) Without ferrite	0.1–0.27	108	90%	10	Fixed load	Double-source control	Need
[33]	Double coils (S-S) Without ferrite	≥ 0.1	1000	83.7%	10	Fixed load	Primary-side control	No need
This paper	Double coils (S-S) Without ferrite	≥ 0.036	294	91.9%	400	Variable	Primary-side control	No need

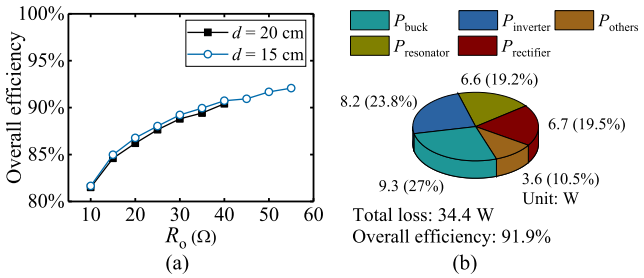

FIGURE 16. Experimental results of overall efficiency and losses when $P_{o,ref} = 400$ W: (a) overall efficiency; (b) loss breakdown of $R_o = 55\Omega$, $d = 15$ cm.

C. ERROR, EFFICIENCY AND LOSSES ANALYSIS

There are errors in load estimated values and output power compared with the actual R_o and reference $P_{o,\,ref}$. It further points out that the errors mainly originate from the assumption that losses of rectifier are ignored during the equation derivation in (25) and (26). If the minor switching losses are neglected and conduction losses are into consideration, the equivalent input resistance R_L seen into the full-bridge rectifier is estimated as

$$R_L \approx \frac{8}{\pi^2} R_o + \frac{4U_f I_f}{I_2^2}, \tag{34}$$

where U_f is the forward voltage of the rectifier diode, I_f is the average forward current of each diode, and I_2 is the RMS value of the secondary-side AC current [35]. Actually, due to the losses of the rectifier, a part of the power obtained by R_L are consumed by the rectifier. Thus, the power delivered to R_o decreases which causes the errors finally. The losses of the rectifier are variable because the average forward current I_f is not constant with different R_o. At the same output power level, the I_f decreases and the loss reduce as the R_o increases, thereby the error decreasing. On the other hand, the measurement noise also has some influence on accuracy. The proposed strategy can be further explored to improve accuracy.

The overall efficiency is calculated by P_{in}/P_o, where P_{in} is the system input power read from DC power supply directly. As shown in Fig. 16(a), the maximum overall efficiency is 91.9% at $R_o = 55\Omega$ when $P_{o,\,ref} = 400$ W. Generally, system losses mainly consist of buck converter losses P_{buck}(switching & conduction losses), inverter losses $P_{inverter}$ (switching & conduction losses), resonator losses $P_{resonator}$, rectifier losses $P_{rectifier}$ (switching & conduction losses) and other losses P_{others}. The system losses are measured at the maximum overall efficiency point, the results of which are plotted in Fig. 16(b). It shows that the losses P_{buck} and $P_{inverter}$ account for a large proportion of system losses. Hence, the design of the inverter and buck converter is vital to improving system performance.

D. COMPARISON WITH EXISTING METHODS

Table 3 compares the performances of output power stabilization control methods for WPT systems reported in recent years. The key introduces of their systems are listed in the table. Unlike the existing methods, the output power stabilization control strategy proposed in this paper considers the variation both of the load and coupling coefficient, and the stable values of output power can be flexibly regulated according to the load identification results, without the need for the information of mutual inductance and the secondary-side measuring or control circuit. According to the table, the WPT system with the control strategy proposed in this paper has competitive advantages due to its flexibility, simplicity and high power-efficiency.

V. CONCLUSION

In this paper, a novel primary-side-only control strategy that realizes stable output power against the variation both of load and coupling condition is proposed for series-series compensated WPT system. The output power is coupling-independent in the exact *PT*-symmetric region and can be stabilized at specified values when the load varies. The proposed strategy has the advantage of eliminating the need for coupling information, dual-side wireless communication, as well as secondary-side control circuits, which simplifies the control algorithm and makes the receiver compact and lightweight. Experimental results validate the performance of the proposed control strategy and system with enough accuracy and high overall efficiency. This paper provides a simple but effective solution to restrain output power fluctuation, and it is suitable for applications such as constant power

charging, dynamic powering and kitchen heating appliance, where the stable and flexible output power is needed with a variation of load and some degree of free positioning.

REFERENCES

[1] P. Si, A. P. Hu, S. Malpas, and D. Budgett, "A frequency control method for regulating wireless power to implantable devices," *IEEE Trans. Biomed. Circuits Syst.*, vol. 2, no. 1, pp. 22–29, Mar. 2008, doi: 10.1109/TBCAS.2008.918284.

[2] X. Shu, W. Xiao, and B. Zhang, "Wireless power supply for small household appliances using energy model," *IEEE Access*, vol. 6, pp. 69592–69602, 2018, doi: 10.1109/access.2018.2880746.

[3] S. Y. Hui, "Planar wireless charging technology for portable electronic products and qi," *Proc. IEEE*, vol. 101, no. 6, pp. 1290–1301, Jun. 2013, doi: 10.1109/jproc.2013.2246531.

[4] T. Kan, F. Lu, T.-D. Nguyen, P. P. Mercier, and C. C. Mi, "Integrated coil design for EV wireless charging systems using LCC compensation topology," *IEEE Trans. Power Electron.*, vol. 33, no. 11, pp. 9231–9241, Nov. 2018, doi: 10.1109/TPEL.2018.2794448.

[5] K. Song, Z. Li, J. Jiang, and C. Zhu, "Constant current/voltage charging operation for series–series and series–parallel compensated wireless power transfer systems employing primary-side controller," *IEEE Trans. Power Electron.*, vol. 33, no. 9, pp. 8065–8080, Sep. 2018, doi: 10.1109/TPEL.2017.2767099.

[6] N. K. Poon, B. M. H. Pong, and C. K. Tse, "A constant-power battery charger with inherent soft switching and power factor correction," *IEEE Trans. Power Electron.*, vol. 18, no. 6, pp. 1262–1269, Nov. 2003, doi: 10.1109/TPEL.2003.818823.

[7] A. Kuperman, U. Levy, J. Goren, A. Zafransky, and A. Savernin, "Battery charger for electric vehicle traction battery switch station," *IEEE Trans. Ind. Electron.*, vol. 60, no. 12, pp. 5391–5399, Dec. 2013, doi: 10.1109/TIE.2012.2233695.

[8] S. Li, L. Wang, Y. Guo, C. Tao, and L. Ji, "Power stabilization with double transmitting coils and T-type compensation network for dynamic wireless charging of EV," *IEEE J. Emerg. Sel. Topics Power Electron.*, early access, May 8, 2019, doi: 10.1109/jestpe.2019.2915551.

[9] S. Wang, J. Chen, Z. Hu, C. Rong, and M. Liu, "Optimisation design for series-series dynamic WPT system maintaining stable transfer power," *IET Power Electronics*, vol. 10, no. 9, pp. 987–995, 2017, doi: 10.1049/iet-pel.2016.0839.

[10] Y. Azadeh, E. Babaei, H. Tarzamni, and M. Sabahi, "Single-Inductor Dual-Output DC-DC Converter With Capability of Feeding a Constant Power Load in Open-Loop Manner," *IEEE Transactions on Industrial Electronics*, vol. 66, no. 9, pp. 6906–6915, 2019, doi: 10.1109/TIE.2018.2880715.

[11] Y. Zhang, T. Kan, Z. Yan, and C. C. Mi, "Frequency and Voltage Tuning of Series-Series Compensated Wireless Power Transfer System to Sustain Rated Power Under Various Conditions," *Ieee J Em Sel Top P*, vol. 7, no. 2, pp. 1311–1317, 2019, doi: 10.1109/JESTPE.2018.2871636.

[12] Wireless Power Consortium. *Ki Cordless Kitchen: From Concept to Industry Standard*. Accessed: Jan. 19, 2020. [Online]. Available: https://www.wirelesspowerconsortium.com/data/downloadables/2/3/7/5/ki-cordless-kitchen-white-paper-september-2019.pdf

[13] M. Kato, T. Imura, and Y. Hori, "New characteristics analysis considering transmission distance and load variation in wireless power transfer via magnetic resonant coupling," in *Proc. Intelec*, Scottsdale, AZ, USA, Sep. 2012, pp. 1–5.

[14] Y. Cao and J. A. A. Qahouq, "Evaluation of maximum system efficiency and maximum output power in two-coil wireless power transfer system by using modeling and experimental results," in *Proc. IEEE Appl. Power Electron. Conf. Expo. (APEC)*, Tampa, FL, USA, Mar. 2017, pp. 1625–1631.

[15] D. van Wageningen and T. Staring, "The Qi wireless power standard," in *Proc. 14th Int. Power Electron. Motion Control Conf. EPE-PEMC*, Ohrid, Macedonia, Sep. 2010, pp. S15-25–S15-32.

[16] N. Y. Kim, K. Y. Kim, J. Choi, and C.-W. Kim, "Adaptive frequency with power-level tracking system for efficient magnetic resonance wireless power transfer," *Electron. Lett.*, vol. 48, no. 8, p. 452, 2012, doi: 10.1049/el.2012.0580.

[17] M. Moghaddami, A. Sundararajan, and A. I. Sarwat, "A power-frequency controller with resonance frequency tracking capability for inductive power transfer systems," *IEEE Trans. Ind. Appl.*, vol. 54, no. 2, pp. 1773–1783, Mar. 2018, doi: 10.1109/TIA.2017.2779425.

[18] S. Liu, M. Liu, S. Han, X. Zhu, and C. Ma, "Tunable class E^2 DC–DC converter with high efficiency and stable output power for 6.78-MHz wireless power transfer," *IEEE Trans. Power Electron.*, vol. 33, no. 8, pp. 6877–6886, Aug. 2018, doi: 10.1109/TPEL.2017.2762924.

[19] S. Assawaworrarit, X. Yu, and S. Fan, "Robust wireless power transfer using a nonlinear parity–time-symmetric circuit," *Nature*, vol. 546, no. 7658, pp. 387–390, Jun. 2017, doi: 10.1038/nature22404.

[20] X. Dai, X. Li, Y. Li, and A. P. Hu, "Impedance-matching range extension method for maximum power transfer tracking in IPT system," *IEEE Trans. Power Electron.*, vol. 33, no. 5, pp. 4419–4428, May 2018, doi: 10.1109/TPEL.2017.2716968.

[21] B. Bo, C. Xu, M. Zhang, R. Wang, and J. Xu, "Output power stabilization control strategy of WPT systems based on secondary side circuit," in *Proc. J. Phys., Conf.* , vol. 1311, Sep. 2019, Art. no. 012018, doi: 10.1088/1742-6596/1311/1/012018.

[22] T. Orekan, P. Zhang, and C. Shih, "Analysis, design, and maximum power-efficiency tracking for undersea wireless power transfer," *IEEE J. Emerg. Sel. Topics Power Electron.*, vol. 6, no. 2, pp. 843–854, Jun. 2018, doi: 10.1109/JESTPE.2017.2735964.

[23] T. Diekhans and R. W. De Doncker, "A dual-side controlled inductive power transfer system optimized for large coupling factor variations and partial load," *IEEE Trans. Power Electron.*, vol. 30, no. 11, pp. 6320–6328, Nov. 2015, doi: 10.1109/tpel.2015.2393912.

[24] L. Tan, Z. Zhang, Z. Zhang, B. Deng, M. Zhang, J. Li, and X. Huang, "A segmented power-efficiency coordinated control strategy for bidirectional wireless power transmission systems with variable structural parameters," *IEEE Access*, vol. 6, pp. 40289–40301, 2018, doi: 10.1109/ACCESS.2018.2852638.

[25] Q. Zhao, A. Wang, J. Liu, and X. Wang, "The load estimation and power tracking integrated control strategy for dual-sides controlled LCC compensated wireless charging system," *IEEE Access*, vol. 7, pp. 75749–75761, 2019, doi: 10.1109/ACCESS.2019.2922329.

[26] H. Liu, X. Huang, D. Czarkowski, L. Tan, J. Li, M. Zhang, and Z. Zhang, "Flexible power control for wireless power transmission system with unfixed receiver position," *IEEE Access*, vol. 7, pp. 181767–181777, 2019, doi: 10.1109/access.2019.2902411.

[27] F. Liu, Z. Ding, X. Fu, and R. M. Kennel, "Parametric optimization of a three-phase MCR WPT system with cylinder-shaped coils oriented by soft-switching range and stable output power," *IEEE Trans. Power Electron.*, vol. 35, no. 1, pp. 1036–1044, Jan. 2020, doi: 10.1109/TPEL.2019.2914154.

[28] M. Su, Z. Liu, Q. Zhu, and A. P. Hu, "Study of maximum power delivery to movable device in omnidirectional wireless power transfer system," *IEEE Access*, vol. 6, pp. 76153–76164, 2018, doi: 10.1109/ACCESS.2018.2883503.

[29] L. Tan, J. Guo, X. Huang, H. Liu, W. Wang, C. Yan, and M. Zhang, "Coordinated source control for output power stabilization and efficiency optimization in WPT systems," *IEEE Trans. Power Electron.*, vol. 33, no. 4, pp. 3613–3621, Apr. 2018, doi: 10.1109/TPEL.2017.2710088.

[30] W. Wang, X. Huang, J. Guo, H. Liu, C. Yan, and L. Tan, "Power stabilization based on efficiency optimization for WPT systems with single relay by frequency configuration and distribution design of receivers," *IEEE Trans. Power Electron.*, vol. 32, no. 9, pp. 7011–7024, Sep. 2017, doi: 10.1109/TPEL.2016.2626498.

[31] J. Schindler, Z. Lin, J. M. Lee, H. Ramezani, F. M. Ellis, and T. Kottos, "PT-symmetric electronics," *J. Phys. A, Math. Theor.*, vol. 45, no. 44, Oct. 2012, Art. no. 444029, doi: 10.1088/1751-8113/45/44/444029.

[32] P.-Y. Chen, M. Sakhdari, M. Hajizadegan, Q. Cui, M. M.-C. Cheng, R. El-Ganainy, and A. Alù, "Generalized parity–time symmetry condition for enhanced sensor telemetry," *Nature Electron.*, vol. 1, no. 5, pp. 297–304, 2018, doi: 10.1038/s41928-018-0072-6.

[33] J. Zhou, B. Zhang, W. Xiao, D. Qiu, and Y. Chen, "Nonlinear Parity-Time-Symmetric model for constant efficiency wireless power transfer: Application to a Drone-in-Flight wireless charging platform," *IEEE Trans. Ind. Electron.*, vol. 66, no. 5, pp. 4097–4107, May 2019, doi: 10.1109/TIE.2018.2864515.

[34] W. Zhong and S. Y. R. Hui, "Maximum energy efficiency operation of series-series resonant wireless power transfer systems using on-off keying modulation," *IEEE Trans. Power Electron.*, vol. 33, no. 4, pp. 3595–3603, Apr. 2018, doi: 10.1109/tpel.2017.2709341.

[35] H. Li, J. Li, K. Wang, W. Chen, and X. Yang, "A maximum efficiency point tracking control scheme for wireless power transfer systems using magnetic resonant coupling," *IEEE Trans. Power Electron.*, vol. 30, no. 7, pp. 3998–4008, Jul. 2015, doi: 10.1109/tpel.2014.2349534.

HUANJIE ZHU was born in Tengxian, Guangxi, China, in 1993. He received the B.S. degree in electrical engineering from the School of Electric Power, South China University of Technology, Guangzhou, China, in 2017, where he is currently pursuing the M.S. degree in power electronics.

His current research interests include wireless power transfer applications and power electronics.

BO ZHANG (Senior Member, IEEE) was born in Shanghai, China, in 1962. He received the B.S. degree in electrical engineering from Zhejiang University, Hangzhou, China, in 1982, the M.S. degree in power electronics from Southwest Jiaotong University, Chengdu, China, in 1988, and the Ph.D. degree in power electronics from the Nanjing University of Aeronautics and Astronautics, Nanjing, China, in 1994.

He is currently a Professor with the School of Electric Power, South China University of Technology, Guangzhou, China. He has authored or coauthored over 450 articles and holds 102 patents. He has authored eight monographs. His research interests include wireless power transfer technology and nonlinear analysis and control of power supplies.

LIHAO WU was born in Gutian, Fujian, China, in 1994. He received the B.S. degree in electrical engineering from Fuzhou University, Fuzhou, China, in 2017. He is currently pursuing the Ph.D. degree in power electronics with the School of Electric Power, South China University of Technology, Guangzhou, China.

His research interests include wireless power transfer applications and power electronic converters.